

Highly Tunable Ground and Excited State Excitonic Dipoles in Multilayer 2H-MoSe₂

Shun Feng,^{1,*} Aidan Campbell,^{1,*} Mauro Brotons-Gisbert,^{1,†} Daniel Andres-Penares,¹ Hyeonjun Baek,¹ Takashi Taniguchi,² Kenji Watanabe,³ Bernhard Urbaszek,⁴ Iann C. Gerber,⁵ and Brian D. Gerardot^{1,‡}

¹*Institute of Photonics and Quantum Sciences, SUPA, Heriot-Watt University, Edinburgh EH14 4AS, UK*

²*International Center for Materials Nanoarchitectonics, National*

Institute for Materials Science, 1-1 Namiki, Tsukuba 305-0044, Japan

³*Research Center for Functional Materials, National Institute for Materials Science, 1-1 Namiki, Tsukuba 305-0044, Japan*

⁴*Institute of Condensed Matter Physics, Technische Universität Darmstadt, 64289 Darmstadt, Germany*

⁵*Université de Toulouse, INSA-CNRS-UPS, LPCNO, 135 Avenue de Rangueil, 31077 Toulouse, France*

(Dated: January 23, 2023)

The fundamental properties of an exciton are determined by the spin, valley, energy, and spatial wavefunctions of the Coulomb bound electron and hole. In van der Waals materials, these attributes can be widely engineered through layer stacking configuration to create highly tunable interlayer excitons with static out-of-plane electric dipoles, at the expense of the strength of the oscillating in-plane dipole responsible for light-matter coupling. Here we show that interlayer excitons in bi- and tri-layer 2H-MoSe₂ crystals exhibit electric-field-driven coupling with the ground ($1s$) and excited states ($2s$) of the intralayer A excitons. We demonstrate that the hybrid states of these distinct exciton species provide strong oscillator strength, large permanent dipoles (up to 0.73 ± 0.01 enm), high energy tunability (up to ~ 200 meV), and full control of the spin and valley characteristics such that the exciton g-factor can be manipulated over a large range (from -4 to $+14$). Further, we observe the bi- and tri-layer excited state ($2s$) interlayer excitons and their coupling with the intralayer excitons states ($1s$ and $2s$). Our results, in good agreement with a coupled oscillator model with spin (layer)-selectivity and beyond standard density functional theory calculations, promote multilayer 2H-MoSe₂ as a highly tunable platform to explore exciton-exciton interactions with strong light-matter interactions.

I. INTRODUCTION

A range of exotic collective effects are predicted to arise from dipolar interactions [1, 2], which have a quadratic dependence on the magnitude of the static electric dipoles (p). For example, strong dipolar interactions may result in exciton crystals, which exhibit ordering due to a balance between exciton kinetic energy and many-body Coulomb interactions [3–7], or lead to nonlinear exciton switches which can reach the quantum limit when the strength of the interaction is larger than the exciton’s radiative linewidth [8–10]. Hence, in the solid-state, much emphasis has been placed on engineering interlayer excitons with large p in pioneering III-V heterostructures [11] and more recently in transition metal dichalcogenide (TMD) heterostructures [12–14] which host excitons with huge binding energies and thus small Bohr radii [15, 16] that enable high exciton densities [17, 18]. In TMD heterostructure devices, tunable interlayer excitons with large p have been realized in homobilayers [19–29] and heterobilayers [30–33], even at the single exciton level [34–36]. However, many of the exotic collective effects underpinned by strong dipolar interactions remain to be observed, motivating further exploration of interlayer excitons and ways to manipulate their spin and optical

properties. For example, it is desirable to increase the electron-hole spatial separation beyond the interlayer distance, but not at the cost of vanishing oscillator strength. This goal is intrinsically difficult for bare interlayer exciton states (e.g. in TMD heterobilayers with Type II interfaces). Recent experimental and theoretical efforts [21, 23, 37] suggest that each ‘bare exciton’ is actually composed of a mixture of other exciton wave functions, and their mixture can be tuned by detuning energy between transitions. Here we use the term bare exciton to denote the majority of each transition for simplicity. While previous studies focused on hybrid interlayer excitons formed in adjacent ‘natural’ homobilayers [21–23], an open question remains if larger hybrid interlayer dipoles, with the electron and hole highly confined in separate layers, can be generally obtained in multilayer TMD platforms. Further, due to the decreasing oscillator strengths of excited Rydberg-like states [15, 16, 38], the observation of excited states of interlayer excitons has proven elusive to date. Characterisation of the excited state spectrum of interlayer excitons provides additional information about their basic properties and a potential means to further engineer dipolar interactions by taking advantage of their larger Bohr radii, which has been crucial to realize optical nonlinearity [39] and excitonic analogues of spatially ordered structures in ultracold atomic gases [40]. To address these issues, we take advantage of hybridised excitons in bilayer (2L) and trilayer (3L) 2H-MoSe₂ composed of the bare exciton states of the interlayer excitons (both $1s$ and $2s$) and the ground ($1s$) and excited ($2s$) states of the intralayer A-excitons. We si-

*These two authors contributed equally

†Electronic address: m.brotons_i_gisbert@hw.ac.uk

‡Electronic address: B.D.Gerardot@hw.ac.uk

multaneously demonstrate strong oscillator strength and wide tunability of the fundamental properties (spin, valley, energy, and spatial wavefunction) of the hybrid exciton species in multilayer MoSe₂.

II. RESULTS AND DISCUSSION

A. Device structure and introduction to excitons in multilayer 2H-MoSe₂

Fig. 1a shows a sketch of our device, which consists of a terraced 2H-MoSe₂ flake with bilayer (2L) and trilayer (3L) regions encapsulated by hexagonal boron nitride (h-BN) layers with nearly identical thicknesses (~ 18 nm). Graphene layers act as electrical contacts for the MoSe₂ crystal and the top and bottom gates (see Suppl. Note S1 for further details of the device fabrication). In our experiments, the MoSe₂ contact is grounded while we apply voltages to the top and bottom gates, labeled as V_T and V_B , respectively. This configuration allows us to apply a vertical electric field with a magnitude V_E (where $V_E = V_B = -V_T$) while keeping the carrier concentration in the MoSe₂ sample constant at charge neutrality. Similar to other TMDs, each layer in our terraced 2H-MoSe₂ flake hosts tightly bound intralayer excitons with both ground ($1s$) and excited ($2s$, $3s$, etc) states [15]. Ground and excited intralayer exciton states present the same exact spin-valley configuration. In the case of the lowest energy excitons in MoSe₂ (the so called A excitons, X^A), both the ground and excited exciton states originate from Coulomb-bound electron-hole pairs in the lower- (higher-) lying conduction (valence) band at $\pm K$ (see Fig. 1b), respectively, which endows them with the same optical selection rules: excitons at $\pm K$ couple to σ^\pm -polarised light [41]. In addition to X^A , there are intralayer B excitons (X^B) composed of the electron (hole) at the top (bottom) of the conduction (valence) band at $\pm K$ respectively, with a considerable energy difference and opposite spin index compared to X^A .

Beyond intralayer exciton states, multilayer TMDs also host interlayer excitons, in which the layer-localised electron wave functions can bind to holes with wave functions confined predominantly within adjacent layers or spread across several layers, giving rise to excitons with spatially extended wave functions [19, 21–25]. Interlayer and intralayer excitons have been shown to coexist in multilayer [20] and bilayer 2H-MoSe₂ [24]. Figure 1a shows a sketch of the possible intra- and interlayer exciton spatial configurations in our terraced 2L/3L 2H-MoSe₂, where we have assumed that, despite the possible spatial spread of the carrier wave functions, the carriers are predominantly confined to a single layer. This assumption leads to three different bare exciton species: i) intralayer excitons within each individual layer (i.e., ground and excited states of the A and B exciton series in MoSe₂ [42]); ii) interlayer excitons with the carriers residing in adjacent layers (IX_{2L}), in which the electron and hole occupy the

upper spin-orbit-split conduction band and the topmost valence band of each layer, respectively (see Fig. 1b); and iii) interlayer excitons in which the carriers reside in the outermost layers of the 3L MoSe₂ region (IX_{3L}), where the electron (hole) occupies the lowermost (topmost) conduction (valence) band (see Fig. 1b). In the 3L MoSe₂ region, IX_{2L} can be formed with carriers from the middle MoSe₂ layer (L_2) and carriers from either the bottom (L_1) or top (L_3) MoSe₂ layers. Note that, despite the spatially indirect character of IX_{2L} and IX_{3L} , these interlayer exciton species exhibit momentum-direct (intravalley) optical transitions within $\pm K$. Moreover, the vertical displacement of the electron and hole wave functions of the bare interlayer excitons results in an out-of-plane static electric dipole (negligible for intralayer excitons), with a dipole polarity and magnitude that depend on the positions and the spatial separation of the electron and hole in the multilayer, respectively (see Fig. 1a). Such out-of-plane permanent electric dipoles of interlayer excitons in other TMD multilayers, homostructures, and heterostructures have been shown to lead to large shifts of the exciton transition energies via the quantum confined Stark effect [21–23, 32, 35, 43]. Finally, the natural 2H stacking of our terraced 2L/3L MoSe₂ flake results in a different relative stacking configuration between the different layers. While IX_{2L} involves MoSe₂ layers with a relative 2H stacking, IX_{3L} originates from MoSe₂ layers with a relative R_h^h -type stacking, where h denotes the hexagon centre of the crystal lattice in each layer (see Fig. 1a). Hence, each IX species is endowed with distinct spin-layer-valley configurations (see Fig. 1b) that can be optically probed. Finally, we note that the relative R_h^h -stacking between L_1 and L_3 is distinct from 3R-stacked homobilayers [27, 44]. For 3R-type bilayers the two layers are laterally shifted so that the hexagon centres in each layer are not vertically aligned, rendering a different symmetry and resulting in a forbidden hole tunneling [45].

B. Electric field dependent excitonic transitions in 2L 2H-MoSe₂

To investigate the layer-dependent and intra-/interlayer nature of the different exciton species in the terraced 2H-MoSe₂ flake, we perform differential reflection contrast ($\Delta R/R_0$) spectroscopy at cryogenic temperature (4 K) as a function of V_E at charge neutrality, where $\Delta R = R_s - R_0$, and R_s (R_0) is the intensity of the light reflected by the flake (substrate). We focus first on the 2L region of our MoSe₂ sample. Supplementary Fig. S1 shows a representative reflection contrast spectrum of our 2L 2H-MoSe₂ at $V_E = 0$ V, where several excitonic resonances with different linewidths and absorption strengths are observed (see Suppl. Fig. S2. for the extracted exciton linewidths). The strongest exciton resonances at low (~ 1.63 eV) and high energy (~ 1.86 eV) correspond to the ground

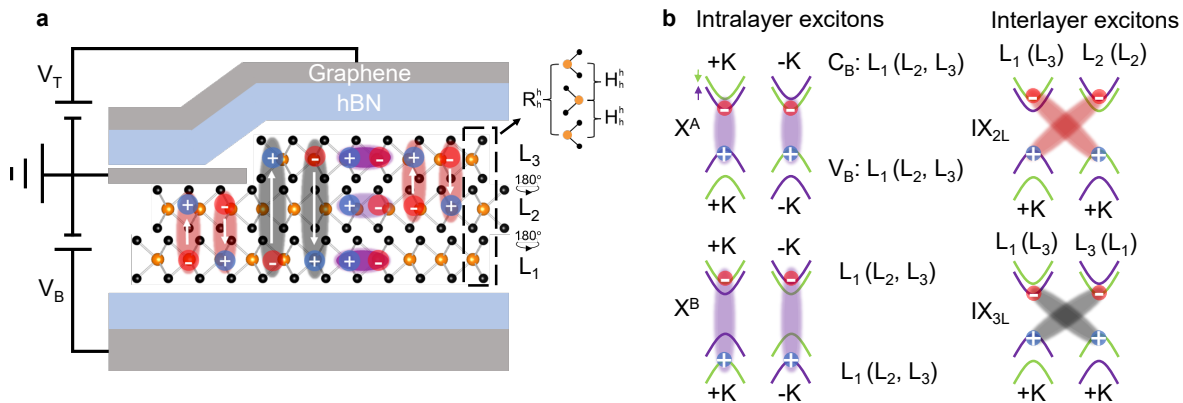


FIG. 1: **Intralayer and interlayer excitons in a terraced 2L/3L 2H-MoSe₂ sample.** **a**, Sketch of the sample and device used in this work: a 2H-MoSe₂ crystal with 2L- and 3L-thick terraces in a dual-gated device configuration. Electrons and holes (red and blue circles, respectively) can be localised either in the bottom (L₁), middle (L₂), or top (L₃) MoSe₂ layers, giving rise to different species of strongly bound intralayer and interlayer excitons. The vertical white arrows indicate the direction of the permanent electric dipoles for the different interlayer excitons. The interlayer stackings are highlighted as R_h^h between L₁ and L₃ and H_h^h between L₁ (L₂) and L₂ (L₃), where h denotes the hexagon center in the crystal lattice of each layer. **b**, Spin-valley configurations of the intralayer and interlayer excitons depicted in panel a: intralayer A and B excitons (purple shaded ovals), and bilayer and trilayer interlayer excitons (red and grey shaded ovals, respectively). The layer labels (L₁-L₃) on each panel indicate the layer origin of the corresponding electronic states in the conduction (C_B) and valence (V_B) bands. The purple (green) bands correspond to spin up (down).

states of intralayer A (X_{1s}^A) and B (X_{1s}^B) neutral excitons in 2L MoSe₂, respectively. Two additional weaker exciton resonances, separated only by ~ 25 meV, are also observed in the energy range between the A and B intralayer 1s exciton states, which can be attributed to IX_{2L} (~ 1.715 eV) and the first excited exciton state X_{2s}^A of the neutral A exciton (~ 1.74 eV), in agreement with previous experimental and theoretical results on bulk [20] and 2L 2H-MoSe₂ [24]. More precisely, we perform $GW+BSE$ calculations (see Suppl. Note S4 for computational details) and obtain IX_{2L} and X_{2s}^A peaks 0.11 and 0.17 eV above the X_{1s}^A one, respectively (see Suppl. Fig. S3), which qualitatively agrees with our experiment in which IX_{2L} and X_{2s}^A are 0.07 and 0.11 eV above X_{1s}^A . To corroborate the intra-/interlayer character of the IX_{2L} and X_{2s}^A states and unravel their layer-dependent properties, we show in Fig. 2a a density plot of the V_E -dependence of the first derivative of the reflectance contrast spectra with respect to photon energy ($d(\Delta R/R_0)/dE$) in the spectral range 1.68 - 1.78 eV, which helps to visualise these exciton transitions (see Suppl. Fig. S4 for comparison with bare $\Delta R/R_0$ spectra). At $V_E = 0$ V, we observe the two excitonic resonances attributed to IX_{2L} and X_{2s}^A . The application of a V_E leads to a stark contrast in the behaviour of the two resonance peaks. For small positive applied V_E , the resonance energy of the high energy peak remains almost constant, while the low energy peak splits into two exciton branches which shift symmetrically towards lower and higher energies with a linear dependence with V_E . This phenomenon can be interpreted in terms

of the DC Stark energy (ΔU) tuning experienced by interlayer excitons under applied out-of-plane electric fields: $\Delta U = -pE$, with E the strength of the vertical electric field and $p = ed$ the out-of-plane electric dipole moment (where e represents the electron charge and d the electron-hole distance). The absolute values of the energy shifts of the two IX_{2L} branches allow us to estimate an average electron-hole spatial separation of $d = 0.34 \pm 0.01$ nm for IX_{2L} , which is comparable to the reported values of 0.39-0.47 nm for IXs in other TMD homostructures such as 2L MoS₂ [22, 23], and 0.63 nm (0.26 nm) for momentum direct (indirect) IXs in twisted bilayer MoSe₂ [28]. This result unambiguously demonstrates the presence of a sizeable static electric dipole in the out-of-plane direction and corroborates the interlayer exciton nature of IX_{2L} [20, 24]. Moreover, the symmetrical but opposite energy shifts of the two IX_{2L} branches reveal the presence of IX_{2L} excitons with different polarities (i.e., with static electric dipoles aligned parallel and anti-parallel to the applied electric field), as sketched in Fig. 1a. For positive V_E , IX_{2L} excitons shifting to lower (higher) energies originate from Coulomb-bound electron-hole pairs in which the hole is spatially located in the top (bottom) layer of the 2L MoSe₂, i.e., with static electric dipoles pointing up (IX_{2L}^{\uparrow}) and down (IX_{2L}^{\downarrow}), respectively. Note that for negative V_E , the behaviour of $IX_{2L}^{\uparrow(\downarrow)}$ is reversed. Therefore, the Stark shifts of $IX_{2L}^{\uparrow(\downarrow)}$ allow us to unravel their layer configuration.

Further, the large DC Stark tuning of IX_{2L} allows us to explore the possible hybridisation between IX_{2L} and

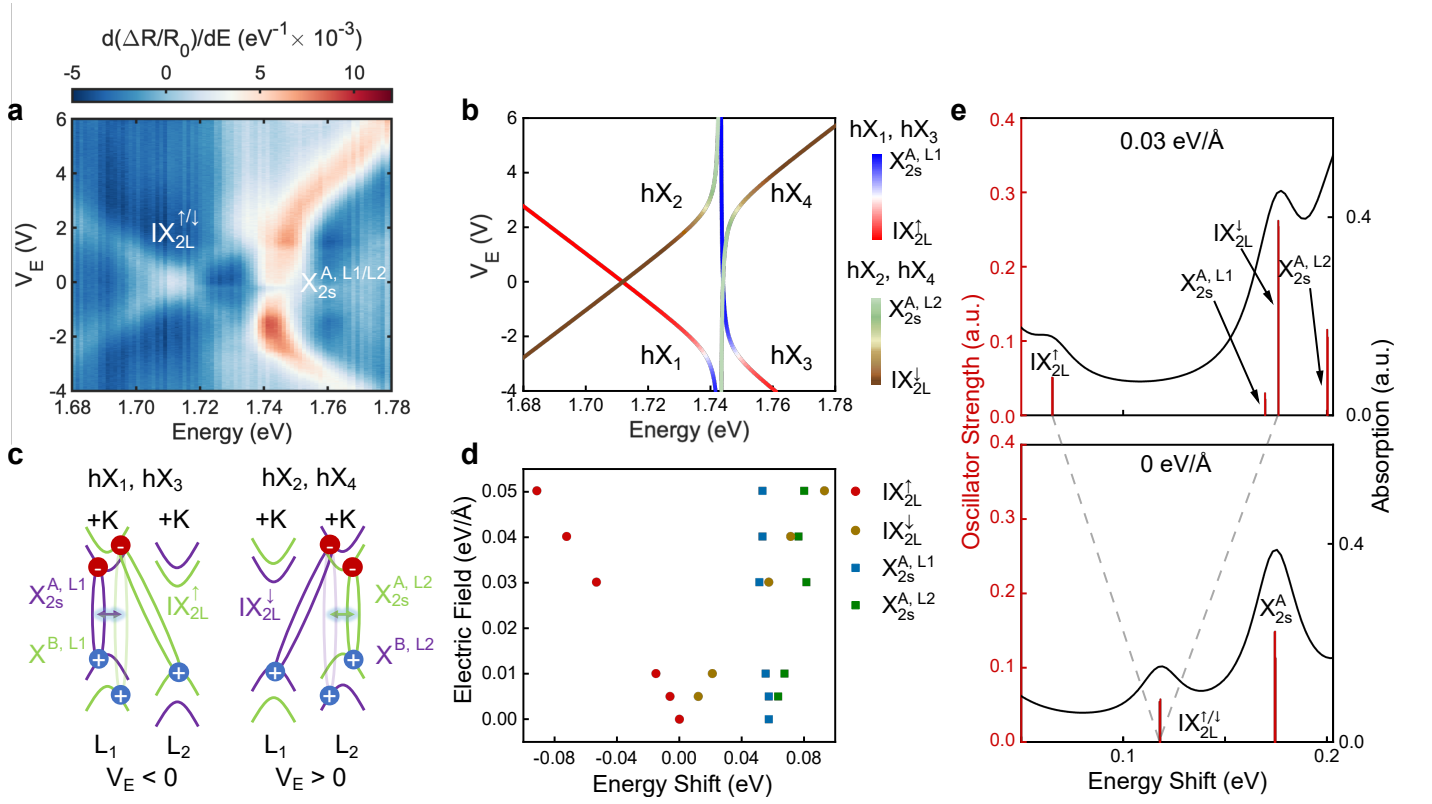


FIG. 2: **Layer hybridised excitons in 2L 2H-MoSe₂.** **a**, V_E dependence of the first derivative of the reflectance contrast spectra with respect to photon energy ($d(\Delta R/R_0)/dE$) in our 2L 2H-MoSe₂ in the spectral range 1.68 - 1.78 eV. **b**, Calculated energies of the different hybrid IX_{2L} - X_{2s}^A exciton states as a function of V_E , which we label as hX_1 , hX_2 , hX_3 , and hX_4 from low to high energy at $V_E > 0$ V, respectively. The colour of the solid lines denotes the contribution of the different bare exciton states to each hybrid exciton. **c**, Schematics of the spin, valley, and layer configuration of the exciton states responsible for the exciton hybridisation shown in panel a for negative and positive applied V_E (left and right panels, respectively). The exciton hybridisation is attributed to a second-order effective coupling between IX_{2L} and the intralayer A exciton facilitated via the A and B exciton admixture (depicted by the glowing double arrows). **d**, The energy position of IX_{2L} and X_{2s}^A as a function of applied electric field, as obtained from $GW+BSE$ calculations. The labels identify the simplified bare exciton states. **e** Normalized theoretical oscillator strengths (red vertical line) and absorption spectra (black line) at 0 eV/Å and 0.03 eV/Å focusing on the energy range of IX_{2L} and X_{2s}^A . The numerical precision of our calculations is estimated to be of the order of ± 5 meV, see computational details in Supplementary Note S4.

the energetically close X_{2s}^A by reducing their energy detuning via the applied V_E . For $|V_E| \approx 2$ V, IX_{2L} and X_{2s}^A show an energy anti-crossing characteristic of coupled systems, suggesting the hybridisation of the two exciton species. We note that this observation is reproduced across the 2L 2H-MoSe₂ sample. Supplementary Fig. S5 shows the results for a different spatial location in the 2L 2H-MoSe₂. In order to estimate the magnitude of the coupling between IX_{2L} and X_{2s}^A , we employ a phenomenological model in which the hybridisation between the exciton states is treated as a coupling between oscillators with resonance energies corresponding to the bare exciton states (see Suppl. Section S3 for details). In our model, we take into account the spin, valley, and layer degrees of freedom of each exciton species, which leads

to eight exciton resonances with different spin, valley, and layer properties: two IX_{2L} with opposite polarities ($IX_{2L}^{\uparrow(\downarrow)}$) and momentum-direct transitions at $\pm K$ each, and X_{2s}^A localised in the top ($X_{2s}^{A,L2}$) and bottom ($X_{2s}^{A,L1}$) MoSe₂ layers with momentum-direct optical transitions at $\pm K$ each. Regarding the IX_{2L} - X_{2s}^A hybridisation, we include it in our model as a phenomenological interlayer coupling of holes at $\pm K$, with a magnitude which we assume to be independent of V_E . In our calculations, the energies of the exciton states at $V_E = 0$ V and the slope of the DC Stark shift for $IX_{2L}^{\uparrow(\downarrow)}$ are set to match the corresponding experimental values, while the value of the coupling strength between the exciton states is left as a free parameter that can be tuned to fit our experimental data. Figure 2b shows the calculated energies of the re-

sulting hybrid exciton states as a function of V_E , which we label as hX_1 , hX_2 , hX_3 , and hX_4 from low to high energy at $V_E > 0$ V, respectively. The colour of the solid lines in Fig. 2b denotes the contribution of the different bare exciton states to each hybrid exciton. The phenomenological model captures well the hybridisation-induced renormalisation of the exciton resonance energies with increasing electric field, allowing us to estimate a IX_{2L} - X_{2s}^A coupling strength $\kappa_{2L-2s} \approx 5.2$ meV, which is slightly smaller but of the same order of magnitude as the linewidths of the exciton states at $V_E = 0$ V (see Suppl. Fig. S2).

The physical origin of the observed hybridisation between an interlayer exciton and the first excited state of an intralayer exciton is intriguing, and to the best of our knowledge has not been reported in any other homobilayer TMD system. We discard the possibility of spin-conserving electron hopping between the electron states involved in IX_{2L} and X_{2s}^A , since such interlayer electron hopping is forbidden in 2L 2H-MoSe₂ due to the C_3 symmetry of the d_{z^2} orbitals of the conduction band states at $\pm K$ [45, 46]. However, a recent theoretical work has shown that the application of a vertical electric field can lead to the hybridisation of IX_{2L} and X_{1s}^B in 2L 2H-MoSe₂ via spin-conserving interlayer hole tunneling [47], in agreement with previous experimental and theoretical results for 2L 2H-MoS₂ [23, 48]. Moreover, similar to 2L 2H-MoS₂, the theoretical results in Ref. [47] also suggest a weak admixture between the A and B excitons in 2L 2H-MoSe₂, which leads to a non-vanishing second-order effective hybridisation of IX_{2L} and the intralayer X_{1s}^A exciton. Since X_{1s}^A and X_{2s}^A have the same nature (i.e., same exact spin and valley configuration), we tentatively attribute the observed IX_{2L} - X_{2s}^A hybridisation to a second-order effective coupling between IX_{2L} and the intralayer A exciton facilitated via the A and B exciton admixture (see Fig. 2c) [47, 48]. This result agrees well conceptually with the theoretical modeling in Ref. [47], and leads to a layer selective coupling between IX_{2L} and the intralayer A exciton, as also captured by our phenomenological model (see Fig. 2b). Our estimated value of the coupling strength $\kappa_{2L-2s} \approx 5.2$ meV is very similar to the coupling strength reported for IX_{2L} and X_{1s}^A excitons in 2H-MoS₂, and significantly smaller than the direct coupling between the IX_{2L} and X_{1s}^B excitons in the same 2H-MoS₂ sample [23, 48], which supports our hypothesis.

To further corroborate our hypothesis, we calculate $GW+BSE$ -based estimates of the excitonic transition energies and their corresponding oscillator strengths at various external electric field values (see Figs. 2d to 2e). For vertical applied positive electric fields, the IX_{2L} excitons experience a significant Stark shift, which supports their interlayer nature. The X_{2s}^{A,L_1} remains relatively unchanged, while the X_{2s}^{A,L_2} exhibits an energy shift with the applied electric field, indicative of the layer-selective mixing with the IX_{2L} state. In fact, our calculations reveal a sizeable mixing between IX_{2L} and X_{2s}^{A,L_2} even at

zero applied electric field. Table 1 in Suppl. Section S4 summarises the oscillator strengths of the different bare optical transitions contributing to each excitonic resonance in Figs. 2d and 2e, corresponding to 0 and 0.03 V/Å applied electric fields, respectively.

C. Electric field dependent excitonic transitions in 3L 2H-MoSe₂

To explore the potential for multilayer TMDs to host IX with dipole moments even larger than IX_{2L} and with greater tunability, we optically probe the 3L region of our terraced 2H-MoSe₂ sample at charge neutrality as a function of V_E . Figure 3a shows the V_E -dependence of $d(\Delta R/R_0)/dE$ in the spectral range 1.58 - 1.78 eV (with the values in the energy range 1.66 - 1.78 eV multiplied by a factor 4 for visualisation purposes). The reflectance spectrum at $V_E = 0$ V is markedly different to the one observed in the 2L region (see Fig. 2a). We observe two exciton transitions in the energy range corresponding to X_{1s}^A with an energy splitting of ~ 11 meV, and two exciton resonances in the energy range of IX_{2L} with an energy splitting of ~ 14.5 meV. The resonances at low energy can be attributed to X_{1s}^A excitons localised in the different layers of our sample, in which the lower average permittivity environment of L_1 and L_3 (h-BN/ $L_{1,(3)}$ /MoSe₂) compared to L_2 (MoSe₂/ L_2 /MoSe₂) results in a dielectric-induced energy blue shift for X_{1s}^A excitons in L_1 and L_3 ($X_{1s}^{A,L_1(L_3)}$) compared to X_{1s}^A excitons in L_2 (X_{1s}^{A,L_2}) [49], similar to what has been observed for 3L MoS₂ [23].

To unravel the nature of the excitons in the energy range corresponding to IX_{2L} , we focus on their behaviour as a function of V_E . As shown in Fig. 3a, the application of a vertical electric field gives rise to a Stark-effect-induced splitting of each resonance into two distinct exciton branches which shift symmetrically towards lower and higher energies with a linear dependence with V_E (see comparison between $\Delta R/R_0$ and $d(\Delta R/R_0)/dE$ in Suppl. Fig. S6). For the lower exciton resonance, we estimate an average electron-hole spatial separation of $d = 0.36 \pm 0.01$ nm, which agrees very well with the value found for IX in the 2L region of our sample, confirming its IX_{2L} nature. The energy splitting of the two branches belonging to the higher energy resonance yields an average electron-hole separation of $d = 0.73 \pm 0.01$ nm, which exceeds the interlayer distance of TMD homobilayers [50] and is approximately twice the IX_{2L} dipole size. We therefore identify this resonance as IX_{3L} . Furthermore, the larger Stark shift of IX_{3L} allows us to tune their energy in resonance to X_{1s}^A (see Fig. 3a). For $|V_E| \sim 4$ V we observe a clear avoided crossing between IX_{3L} and $X_{1s}^{A,L_1/L_3}$, indicative of the hybridisation between the exciton species with carriers hosted in the outermost layers of the 3L MoSe₂ sample. Supplementary Fig. S7 shows the results for a different spatial location in the 3L 2H-

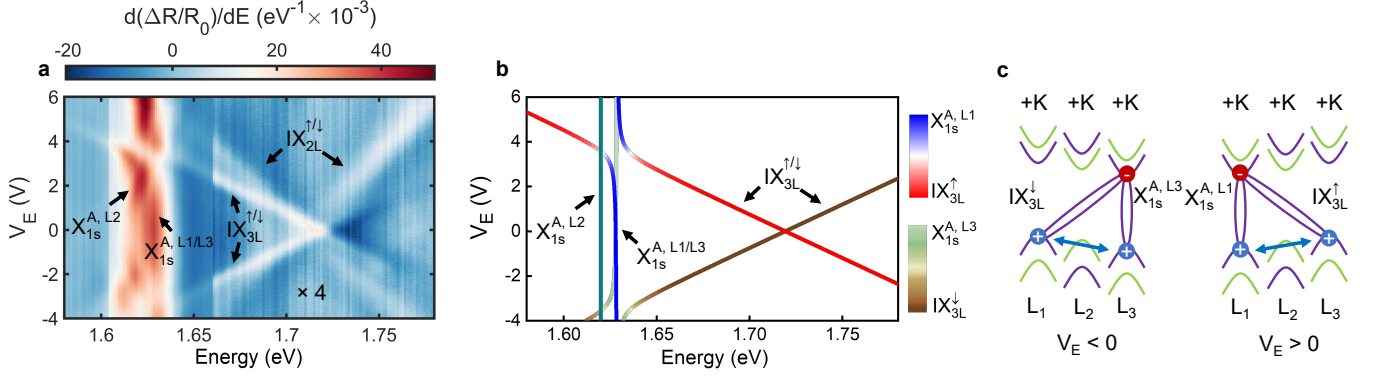


FIG. 3: **Layer hybridised excitons in 3L MoSe₂.** **a**, V_E dependence of $d(\Delta R/R_0)/dE$ in the 3L MoSe₂ region of our sample. **b**, Energies of the different hybrid $IX_{3L}-X_{1s}^A$ exciton states as a function of V_E , where the colour of the solid lines denotes the contribution of the different bare exciton states to each hybrid exciton. **c**, Schematics of the spin, valley, and layer configuration of the exciton states responsible for the exciton hybridisation shown in panel a for negative and positive applied V_E (left and right panels, respectively). The exciton hybridisation is attributed to direct spin-conserving interlayer hole tunnelling between L_1 and L_3 .

MoSe₂. We note that, contrary to the results for the 2L region, we observe negligible oscillator strength of X_{2s}^A in the 3L MoSe₂ region, which prevents clear observation of coupling between this exciton state and the two IX species. Therefore, we focus on the clear $IX_{3L}-X_{1s}^A$ hybridisation.

Similar to the 2L case, we simulate the V_E -dependent energy dispersion of the hybridised excitons in the 3L MoSe₂ system using a phenomenological model of coupled oscillators, in which the exciton coupling is both spin- and layer-selective (see Fig. 3b). In this case, we include three different X_{1s}^A excitons (i.e., one in each layer) and two IX_{3L} with opposite polarities ($IX_{3L}^{\uparrow(\downarrow)}$) and momentum-direct transitions at $\pm K$ each. Spin conserving hole tunneling results in a layer-selective coupling between IX_{3L} and X_{1s}^A ; the polarity of IX_{3L} is locked to the layer degree of freedom of X_{1s}^A (e.g. $IX_{3L}^{\uparrow(\downarrow)}$ only couples to $X_{1s}^{A,L1(L3)}$). However, the energy degeneracy of $X_{1s}^{A,L1}$ and $X_{1s}^{A,L3}$ prevents clear observation of such layer-selective coupling experimentally. Figure 3b shows the results of the best fit of the model to our experimental data. The colour of the solid lines denotes the contribution of the different bare exciton states to each hybrid exciton. Overall, the phenomenological model captures well the hybridisation-induced renormalisation of the exciton resonance energies with increasing electric field, allowing us to estimate a $IX_{3L}-X_{1s}^A$ coupling strength $\kappa_{3L-1s} \approx 7.5$ meV, which is slightly larger but of the same order of magnitude as κ_{2L-2s} in the 2L region. Furthermore, it is worth noting that the R-type relative stacking of the layers L_1 and L_3 leads to some differences between the $IX_{3L}-X_{1s}^A$ and $IX_{2L}-X_{2s}^A$ couplings. The R-type stacking between L_1 and L_3 results in IX_{3L} with electron-hole pairs with the same spin-valley configurations as X^A (see Fig. 1a), which allows the hybridisation of the two exci-

ton species via direct spin-conserving interlayer hole tunnelling in the presence of an additional layer between L_1 and L_3 [29, 51]. For the specific stacking registry of R_h^h between L_1 and L_3 , a recent work calculated an 11 meV tunnel splitting of the valence band (with monolayer BN as L_2) [29], supporting our interpretation. On the contrary, due to the $2H$ relative stacking between adjacent layers, the direct hole tunneling between the valence band states in IX_{2L} and X^A has to compete with a sizable detuning equal to the spin splitting at the valence band edges (150 meV in MoSe₂ [51]), and is thus only facilitated by the admixture of X^A and X^B . Finally, we note that the energy detuning between IX_{2L} and the energy degenerate $X_{1s}^{A,L1}$ and $X_{1s}^{A,L3}$ exciton resonances is slightly smaller in the 3L region as compared to the 2L one. As a consequence, we are able to observe experimental signatures of the coupling between these two exciton species at $V_E \sim 6$ V (see Fig. 3a and Suppl. Section S6), which corroborate our results for the 2L 2H-MoSe₂.

D. Electric-field-dependent magneto-optical properties of hybrid excitons in MoSe₂

Beyond tuning of the exciton resonance energies, oscillator strengths, and effective permanent electric dipoles, here we explore if the electric-field-dependent control of the exciton nature enables precision tuning of the effective Landé g -factors. The application of a vertical magnetic field B results in the Zeeman splitting of the optical transitions of each exciton at $\pm K$, with an energy splitting $\Delta E(B) = g\mu_0 B$, with μ_0 the Bohr magneton. Optical transitions at $\pm K$ can be independently probed by σ^\pm -polarised light, respectively, which enables us to perform circularly polarised reflectance contrast measurements to estimate the experimental Zeeman splitting

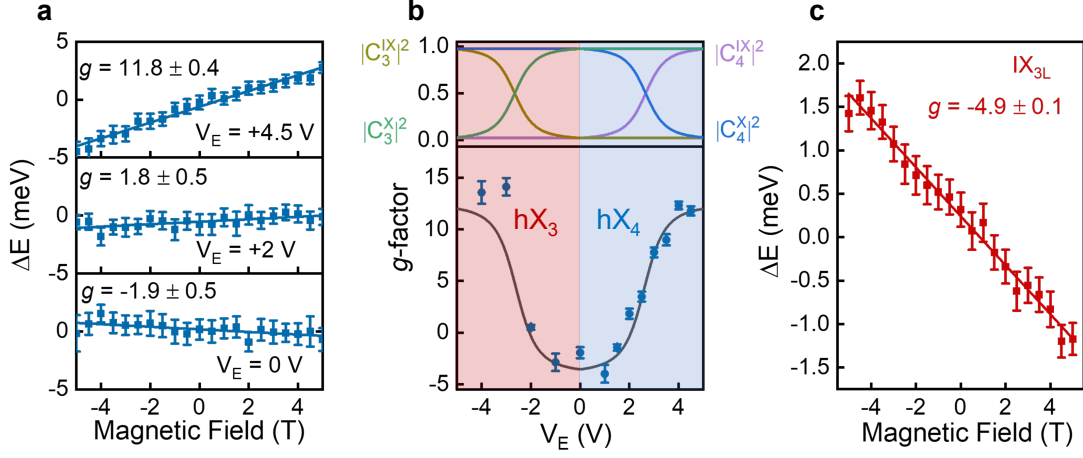


FIG. 4: **Magneto-optical properties of layer-hybridised excitons in 2L MoSe₂ and 3L MoSe₂.** **a**, Zeeman splitting of hX_4 at three different applied V_E . The blue dots represent the experimental values, while the blue solid lines show linear fits of the experimental data, from which we are able to estimate the effective g -factor of this hybrid exciton at each applied V_E . **b**, V_E -driven evolution of the g -factor of the hybrid excitons hX_3 (-5 to 0 V, red shaded area) and hX_4 (0 to 5 V, blue shaded area) in bilayer MoSe₂ (bottom panel). The top panel shows the V_E -dependent contributions of each bare exciton state $|C_{3,4}^{IX(X)}|^2$ to the corresponding hybrid excitons. **c**, Zeeman splitting of IX_{3L} at measured at $V_E = 0$ V.

$\Delta E = E^{\sigma^+} - E^{\sigma^-}$, with E^{σ^\pm} the energy of the σ^\pm -polarised transition. We focus first on the hybrid IX_{2L} - X_{2s}^A exciton states in our 2L region. Figure 4a shows the measured Zeeman splittings (blue dots) for hX_4 at three different applied V_E values. Supplementary Figure S8 shows the linecuts for the σ^\pm -resolved $d(\Delta R/R_0)/dE$ at $V_E = 0$ V for 5 T. The blue solid lines represent linear fits of the experimental data, from which we estimate the effective g -factor at each applied V_E . We observe the effective g -factor of hX_4 is tuned from a negative value (-1.9 ± 0.5) to a relatively large positive value (11.8 ± 0.4). To explore this effect in more detail, we employ the same experimental procedure and extract the effective g -factors of hX_3 and hX_4 in the range of applied V_E in which the oscillator strength of each transition and their energy detuning with respect to other transitions enable a reliable estimate of E^{σ^\pm} , i.e., $V_E < 0$ for hX_3 and $V_E > 0$ for hX_4 (as indicated by the red and blue shaded areas in Fig. 4b). The results highlight a continuous and smooth transition of the g -factor of the two hybrid exciton states from -1.9 ± 0.5 to 11.8 ± 0.4 by changing V_E from 0 V to ± 4.5 V. Such evolution of the effective g -factor arises from the V_E -dependent hybridisation between IX_{2L} and X_{2s}^A , and can be quantitatively explained by our phenomenological model of coupled oscillators. In this model, the wave function of each hybrid exciton is expressed as a superposition of the bare intralayer and interlayer exciton wave functions (see Suppl. Section S3). In the case of hX_3 and hX_4 , these exciton wave functions are expressed as follows:

$$|hX_3(V_E)\rangle = C_3^{IX}(V_E) |IX_{2L}^\uparrow\rangle + C_3^X(V_E) |X_{2s}^{A,L_1}\rangle \quad (1)$$

and

$$|hX_4(V_E)\rangle = C_4^{IX}(V_E) |IX_{2L}^\downarrow\rangle + C_4^X(V_E) |X_{2s}^{A,L_2}\rangle, \quad (2)$$

where $C_i^{IX(X)}(V_E)$ represents the V_E -dependent amplitude of the bare interlayer (intralayer) exciton state in hybrid exciton state $|hX_i\rangle$, with $|C_i^{IX}(V_E)|^2 + |C_i^X(V_E)|^2 = 1$. Therefore, the effective g -factor of each hybrid exciton state (g_{hX_i}) can be expressed as

$$g_{hX_i}(V_E) = |C_i^{IX}(V_E)|^2 g_{IX_{2L}} + |C_i^X(V_E)|^2 g_{X_{2s}}, \quad (3)$$

where $g_{IX_{2L}(X_{2s})}$ represents the g -factor of the bare IX_{2L} (X_{2s}) state. The solid line in Fig. 4b represents a fit of the experimental data to Eq. (3), in which we have used the $C_i^{IX(X)}(V_E)$ values shown in the top panel of Fig. 4b (obtained from the fits in Fig. 2b), and $g_{IX_{2L}}$ and $g_{X_{2s}}$ have been left as free fitting parameters. Our model captures well the hybridisation-induced evolution of the g -factors and allows us to estimate of the effective g -factors of the bare states: $g_{X_{2s}} \approx -4$ and $g_{IX_{2L}} \approx 12.5$. We note that, although to the best of our knowledge $g_{X_{2s}}$ has not been previously reported for 2L MoSe₂, our estimated value of $g_{X_{2s}}$ is in very good agreement with reported experimental (-3.6 ± 0.1 [52]) and theoretical (-3.7 [53]) values for this excited exciton state in monolayer MoSe₂ and other TMD systems such as bulk WSe₂ (-3.3 ± 0.6 [20]). Regarding $g_{IX_{2L}}$, the estimated sign and value are also in good agreement with the value predicted by a simplistic “atomic picture”, in which the g -factor of the bands hosting the electron-hole pairs are assumed to be equal to the sum of their spin, orbital, and valley magnetic moments

[54]. Within this model, the spin-valley configuration of IX_{2L} results in a $g_{IX_{2L}} = 2(\frac{m_0}{m_c^*} + \frac{m_0}{m_v^*}) + 4 \approx 9.7$, with m_0 the free electron mass, and m_c^* and m_v^* the experimentally reported electron and hole effective masses for the bottom conduction band and top valence band in monolayer $MoSe_2$, respectively [55]. The relatively large and positive value of the g -factor estimated with this atomic picture model provides an additional confirmation of the spin-valley configuration and interlayer nature of IX_{2L} . Also, we note that the small discrepancy between the experimental and the calculated value for $g_{IX_{2L}}$ might arise from a combination of several factors, including the limitation of this simple model to estimate accurately the g -factor of the relevant bands [56] and the absence of experimental values for the electron effective mass of the top conduction band in 2L $MoSe_2$, which theoretical calculations predict to be slightly smaller than for the bottom conduction band in Mo-based TMDs such as 2H- $MoSe_2$ [57] and 2H- MoS_2 [58]. Nevertheless, we note that the extracted g -factors of the bare IX_{2L} and X_{2s} states allow us to include the effects of the Zeeman splitting in the calculated V_E -dependent evolution of the hybrid IX_{2L} - X_{2s} states, for which we find a very good agreement with the experimental results (see Suppl. Note S5 and Suppl. Fig. S12).

Finally, we investigate the magneto-optical properties of IX_{3L} in the 3L region of the sample. Figure 4c shows the experimental Zeeman splitting for this exciton species at $V_E = 0$ V, from which we estimate a g -factor $g_{IX_{3L}} = -4.9 \pm 0.1$. The extracted value for $g_{IX_{3L}}$ is very similar to the experimentally reported g -factor of X_{1s}^A in 3L $MoSe_2$ [56], which confirms the identical spin-valley configuration of these two exciton species and corroborates that the giant dipole IX_{3L} indeed originates from electron and hole in L_1 and L_3 (or vice versa), respectively. The identical spin-valley configuration of X_{1s}^A and IX_{3L} has an important consequence on the magneto-optical properties of the hybrid X_{1s}^A - IX_{3L} states: contrary to the hybrid X_{2s}^A - IX_{2L} states in 2L $MoSe_2$, hybrid X_{1s}^A - IX_{3L} do not feature a V_E -tunable g -factor, since the two bare exciton states already exhibit a similar g -factor.

E. Excited state interlayer excitons in multilayer 2H- $MoSe_2$

Although excited (Rydberg) exciton states have weaker oscillator strength than their corresponding ground states [15], in this section we show that the hybridisation of interlayer excitons with intralayer transitions leads to clear spectroscopic signatures of excited Rydberg states for both IX_{2L} and IX_{3L} . Figures 5a and 5b show $d^2(\Delta R/R_0)/dE^2$ spectra as a function of V_E for 2L and 3L 2H- $MoSe_2$ regions, respectively, corresponding to spatial locations where the interlayer excited exciton states present appreciable oscillator strengths. The data shown in the the spectral ranges 1.797 - 1.830 eV and 1.665 - 1.800 eV in Figs. 5a and 5b have been multiplied

by a factor 2 for visualisation purposes. In the 2L region (Fig. 5a), for $4 \lesssim V_E \lesssim 6$ V we resolve an additional exciton transition in the energy range ~ 1.7 eV with a linear Stark shift parallel to the IX_{2L}^\uparrow . Extrapolation of the linear energy shift to $V_E = 0$ V gives an estimated energy of ~ 1.77 eV for this excitonic transition with clear interlayer nature. We note that the relative energy position of this excitonic peak with respect to both IX_{2L} and X_{2s}^A agrees well with the first excited Rydberg state of IX_{2L} predicted by our GW -BSE results (see Figs. 2e and Suppl. Fig. S3). This, together with the dipole moment of 0.30 ± 0.01 enm estimated from the linear Stark shift (almost identical to the one for IX_{2L}), allows us to attribute the observed resonance to the first excited Rydberg state of IX_{2L}^\uparrow (i.e., $IX_{2s,2L}^\uparrow$). Notably, for $|V_E| \sim 3$ V and energies ~ 1.82 eV, we observe two additional resonances with opposite Stark shift slopes that also extrapolate to an energy of ~ 1.77 eV at $V_E = 0$ V, which we attribute to $IX_{2s,2L}^\downarrow$ ($V_E > 0$ V) and $IX_{2s,2L}^\uparrow$ ($V_E < 0$ V), corroborating our peak assignment. We note that the $IX_{2s,2L}$ state is a general feature rather than a location dependent feature of our sample, as we also observe $IX_{2s,2L}$ in the main locations of 2L and 3L $MoSe_2$ shown in Figs. 2-4, as depicted in Suppl. Fig. S10. Further, we observe a very weak transition near 1.72 eV for $4 \lesssim V_E \lesssim 6$ V with a Stark shift parallel to $IX_{2s,2L}$ (see Suppl. Fig. S9), which we tentatively ascribe as the $3s$ Rydberg state of IX_{2L} . Extrapolation to $V_E = 0$ V gives an estimated energy for the $3s$ state of ~ 20 meV higher than the $2s$ at zero applied electric field.

Similar to Fig. 5a, the results in Fig. 5b also display clear excited Rydberg states in our 3L 2H- $MoSe_2$ sample. In addition to the coexisting interlayer exciton species IX_{2L} and IX_{3L} already shown in Fig. 3, we observe two additional transitions with Stark-induced linear energy shifts parallel to the IX_{3L} , which we attribute to the two opposite polarities of the $2s$ excited Rydberg state of IX_{3L} (i.e., $IX_{2s,3L}^{\uparrow(\downarrow)}$). Extrapolation of the measured linear energy shifts of $IX_{2s,3L}^{\uparrow(\downarrow)}$ to $V_E = 0$ V gives an estimated energy ~ 40 meV above the IX_{3L} ground state (near the X_{2s}^A transition).

Finally, we simulate the V_E -dependent energy dispersions of the hybridised ground and excited exciton Rydberg states using the phenomenological coupled oscillator model previously described. We build on the models used for Figs. 2b and 3b and add the the observed excited Rydberg states, which we assume to have identical Stark shifts and the same spin- and layer-selective couplings than their corresponding ground states. Figures 5c and 5d show the simulated energy dispersions corresponding to the results in Figs. 5a and 5b, respectively. As can be observed in these figures, the simulated energy dispersions capture well the V_E -induced hybridisation and energy dispersion of the different excitonic transitions (see Suppl. Fig. S15 for the the simulated absorption spectrum as a function of V_E corresponding to Figs. 5b using this model and suppl. section 6 for simulation

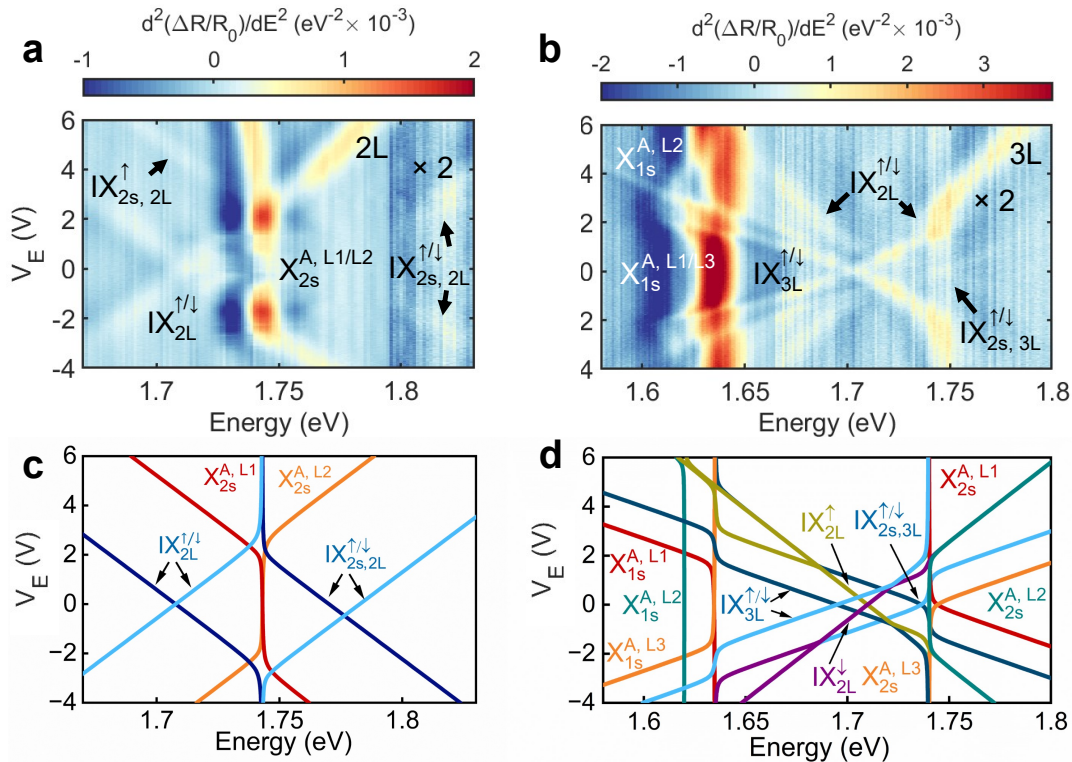


FIG. 5: **Observation of excited states of IX_{2L} and IX_{3L} .** **a**, V_E dependence of $d^2(\Delta R/R_0)/dE^2$ in a second location of the 2L 2H-MoSe₂ sample in the spectral range 1.67 - 1.83 eV. **b**, $d^2(\Delta R/R_0)/dE^2$ in another location of the 3L 2H-MoSe₂ sample in the spectral range 1.58 - 1.8 eV. **c** Calculated energies of the different exciton states of 2L 2H-MoSe₂ including $IX_{2s,2L}$ with same spin and layer configuration as IX_{2L} . **d** Calculated energies of the different exciton states in 3L 2H-MoSe₂ including $IX_{2s,3L}$ with the same spin and layer configuration as IX_{3L} .

details), supporting our interpretation of their different intra-/interlayer origin, ground/excited state character, and spin and valley configurations.

III. SUMMARY AND OUTLOOK

Our work reports the observation of giant Stark splitting of the interlayer excitons in 2L and 3L 2H-MoSe₂. First, we observe hybridisation between IX_{2L} and X_{2s}^A . In addition to their spectral evolution, a hybridisation driven g-factor evolution of the coupled excitons is resolved and understood via a unified coupled oscillator model. The ability to drive the exciton Zeeman splitting from negative to positive through zero has potential in electrically tunable valleytronics and spin-dependent exciton-exciton interactions. Next, we report the giant excitonic trilayer dipole IX_{3L} , which exhibits distinct spin-layer selection rules for hybridisation with X_{1s}^A . A salient feature of the large IX_{3L} dipole is that it can be Stark tuned to become the ground state (e.g. lower energy than X_{1s}^A), promising for applications in exciton transport. Finally, by harnessing the exciton hybridisation affects, we successfully probe the excited state IX for

the first time in a TMD system. Future theory and experimental effort is encouraged to better understand the excited IX states, including comparisons with the hydrogen model and the magnetic field and doping dependence to reveal the g-factor, effective mass [55] and Roton-like [59] properties of the interlayer Rydberg excitons. Altogether, the results promote a new TMD homostructure candidate for applications with enhanced exciton-exciton interactions with strong light-matter coupling. Beyond 3L 2H-MoSe₂, a strategy of further engineering IX dipoles by tuning the layer number, including thicker multilayer ($> 3L$) 2H-TMDs or heterostructures with multilayer TMD components and hBN spacers, is encouraged.

IV. ACKNOWLEDGEMENTS

S.F. and A.C. contributed equally to this work. This work was supported by the EPSRC (grant nos. EP/P029892/1 and EP/L015110/1), the ERC (grant no. 725920). S.F. is supported by a Marie Skłodowska-Curie Individual Fellowship H2020-MSCA-IF-2020 SingExTr (No. 101031596). M.B.-G. is supported by a Royal

Society University Research Fellowship. B.D.G. is supported by a Wolfson Merit Award from the Royal Society and a Chair in Emerging Technology from the Royal Academy of Engineering. K.W. and T.T. acknowledge support from the Elemental Strategy Initiative conducted by the MEXT, Japan (Grant Number JP-

MXP0112101001) and JSPS KAKENHI (Grant Numbers 19H05790, 20H00354 and 21H05233). I.C.G acknowledges the CALMIP initiative for the generous allocation of computational time, through Project No. p0812, as well as GENCI-CINES, GENCI-IDRIS, GENCI-CCRT for Grant No. A012096649.

-
- [1] L. Butov, J. Phys. Condens. Matter **16**, R1577 (2004).
- [2] T. Lahaye, C. Menotti, L. Santos, M. Lewenstein, and T. Pfau, Rep. Prog. Phys **72**, 126401 (2009).
- [3] G. E. Astrakharchik, J. Boronat, I. L. Kurbakov, and Y. E. Lozovik, Phys. Rev. Lett. **98**, 060405 (2007).
- [4] B. Capogrosso-Sansone, N. V. Prokof'ev, and B. V. Svistunov, Phys. Rev. B **75**, 134302 (2007).
- [5] Y. Slobodkin, Y. Mazuz-Harpaz, S. Refaely-Abramson, S. Gazit, H. Steinberg, and R. Rapaport, Phys. Rev. Lett. **125**, 255301 (2020).
- [6] G. Astrakharchik, I. Kurbakov, D. Sychev, A. Fedorov, and Y. E. Lozovik, Phys. Rev. B **103**, L140101 (2021).
- [7] I. V. Bondarev, O. L. Berman, R. Y. Kezerashvili, and Y. E. Lozovik, Commun. Phys. **4**, 134 (2021).
- [8] D. E. Chang, V. Vuletić, and M. D. Lukin, Nat. Photon. **8**, 685 (2014).
- [9] Superlattices and Microstructures **108**, 2 (2017).
- [10] A. Delteil, T. Fink, A. Schade, S. Höfling, C. Schneider, and A. İmamoğlu, Nat. Mater. **18**, 219 (2019).
- [11] A. A. High, J. R. Leonard, A. T. Hammack, M. M. Fogler, L. V. Butov, A. V. Kavokin, K. L. Campman, and A. C. Gossard, Nature **483**, 584 (2012).
- [12] M. Fogler, L. Butov, and K. Novoselov, Nat. Commun. **5**, 4555 (2014).
- [13] D. Erckensten, S. Brem, and E. Malic, Phys. Rev. B **103**, 045426 (2021).
- [14] C. Lagoin and F. m. c. Dubin, Phys. Rev. B **103**, L041406 (2021).
- [15] A. Chernikov, T. C. Berkelbach, H. M. Hill, A. Rigosi, Y. Li, O. B. Aslan, D. R. Reichman, M. S. Hybertsen, and T. F. Heinz, Phys. Rev. Lett. **113**, 076802 (2014).
- [16] K. He, N. Kumar, L. Zhao, Z. Wang, K. F. Mak, H. Zhao, and J. Shan, Phys. Rev. Lett. **113**, 026803 (2014).
- [17] Z. Wang, D. A. Rhodes, K. Watanabe, T. Taniguchi, J. C. Hone, J. Shan, and K. F. Mak, Nature **574**, 76 (2019).
- [18] M. Kulig, J. Zipfel, P. Nagler, S. Blanter, C. Schüller, T. Korn, N. Paradiso, M. M. Glazov, and A. Chernikov, Phys. Rev. Lett. **120**, 207401 (2018).
- [19] A. Arora, M. Drüppel, R. Schmidt, T. Deilmann, R. Schneider, M. R. Molas, P. Marauhn, S. Michaelis de Vasconcellos, M. Potemski, M. Rohlfling, *et al.*, Nat. Commun. **8**, 639 (2017).
- [20] A. Arora, T. Deilmann, P. Marauhn, M. Drüppel, R. Schneider, M. R. Molas, D. Vaclavkova, S. M. de Vasconcellos, M. Rohlfling, M. Potemski, *et al.*, Nanoscale **10**, 15571 (2018).
- [21] N. Peimyoo, T. Deilmann, F. Withers, J. Escolar, D. Nutting, T. Taniguchi, K. Watanabe, A. Taghizadeh, M. F. Craciun, K. S. Thygesen, *et al.*, Nat. Nanotechnol. **16**, 888 (2021).
- [22] E. Lorchat, M. Selig, F. Katsch, K. Yumigeta, S. Tongay, A. Knorr, C. Schneider, and S. Höfling, Phys. Rev. Lett. **126**, 037401 (2021).
- [23] N. Leisgang, S. Shree, I. Paradisanos, L. Sponfeldner, C. Robert, D. Lagarde, A. Balocchi, K. Watanabe, T. Taniguchi, X. Marie, *et al.*, Nat. Nanotechnol. **15**, 901 (2020).
- [24] J. Horng, T. Stroucken, L. Zhang, E. Y. Paik, H. Deng, and S. W. Koch, Phys. Rev. B **97**, 241404 (2018).
- [25] Z. Wang, Y.-H. Chiu, K. Honz, K. F. Mak, and J. Shan, Nano Lett. **18**, 137 (2018).
- [26] Ł. Kipcza, A. O. Slobodeniuk, T. Woźniak, M. Bhatnagar, N. Zawadzka, K. Olkowska-Pucko, M. Grzeszczyk, K. Watanabe, T. Taniguchi, A. Babiński, *et al.*, arXiv preprint arXiv:2211.16186 (2022).
- [27] I. Paradisanos, S. Shree, A. George, N. Leisgang, C. Robert, K. Watanabe, T. Taniguchi, R. J. Warburton, A. Turchanin, X. Marie, *et al.*, Nat. Commun. **11**, 2391 (2020).
- [28] J. Sung, Y. Zhou, G. Scuri, V. Zólyomi, T. I. Andersen, H. Yoo, D. S. Wild, A. Y. Joe, R. J. Gelly, H. Heo, *et al.*, Nat. Nanotechnol. **1**, 1 (2020).
- [29] Y. Shimazaki, I. Schwartz, K. Watanabe, T. Taniguchi, M. Kroner, and A. İmamoğlu, Nature **580**, 472 (2020).
- [30] P. Rivera, J. R. Schaibley, A. M. Jones, J. S. Ross, S. Wu, G. Aivazian, P. Klement, K. Seyler, G. Clark, N. J. Ghimire, *et al.*, Nat. Commun. **6**, 6242 (2015).
- [31] A. Ciarrocchi, D. Unuchek, A. Avsar, K. Watanabe, T. Taniguchi, and A. Kis, Nat. Photon. **13**, 131 (2019).
- [32] L. A. Jauregui, A. Y. Joe, K. Pistunova, D. S. Wild, A. A. High, Y. Zhou, G. Scuri, K. De Greve, A. Sushko, C.-H. Yu, *et al.*, Science **366**, 870 (2019).
- [33] Y. Tang, J. Gu, S. Liu, K. Watanabe, T. Taniguchi, J. Hone, K. F. Mak, and J. Shan, Nat. Nanotechnol. **16**, 52 (2021).
- [34] M. Kremser, M. Brotons-Gisbert, J. Knörzer, J. Gückelhorn, M. Meyer, M. Barbone, A. V. Stier, B. D. Gerardot, K. Müller, and J. J. Finley, NPJ 2D Mater. Appl. **4**, 8 (2020).
- [35] H. Baek, M. Brotons-Gisbert, Z. Koong, A. Campbell, M. Rambach, K. Watanabe, T. Taniguchi, and B. Gerardot, Sci. Adv. **6**, eaba8526 (2020).
- [36] W. Li, X. Lu, S. Dubey, L. Devenica, and A. Srivastava, Nat. Mater. **19**, 624 (2020).
- [37] I. C. Gerber, E. Courtade, S. Shree, C. Robert, T. Taniguchi, K. Watanabe, A. Balocchi, P. Renucci, D. Lagarde, X. Marie, and B. Urbaszek, Phys. Rev. B **99**, 035443 (2019).
- [38] A. V. Stier, N. P. Wilson, K. A. Velizhanin, J. Kono, X. Xu, and S. A. Crooker, Phys. Rev. Lett. **120**, 057405 (2018).
- [39] V. Walther, R. Johne, and T. Pohl, Nat. Commun. **9**, 1309 (2018).
- [40] P. Schauß, M. Cheneau, M. Endres, T. Fukuhara, S. Hild, A. Omran, T. Pohl, C. Gross, S. Kuhr, and I. Bloch,

- Nature **491**, 87 (2012).
- [41] D. Xiao, G.-B. Liu, W. Feng, X. Xu, and W. Yao, Phys. Rev. Lett. **108**, 196802 (2012).
- [42] A. Arora, K. Nogajewski, M. Molas, M. Koperski, and M. Potemski, Nanoscale **7**, 20769 (2015).
- [43] P. Rivera, K. L. Seyler, H. Yu, J. R. Schaibley, J. Yan, D. G. Mandrus, W. Yao, and X. Xu, Science **351**, 688 (2016).
- [44] J. Shi, P. Yu, F. Liu, P. He, R. Wang, L. Qin, J. Zhou, X. Li, J. Zhou, X. Sui, *et al.*, Adv. Mater. **29**, 1701486 (2017).
- [45] Z. Gong, G.-B. Liu, H. Yu, D. Xiao, X. Cui, X. Xu, and W. Yao, Nat. Commun. **4**, 2053 (2013).
- [46] J. Hagel, S. Brem, C. Linderålv, P. Erhart, and E. Malic, Phys. Rev. Res. **3**, 043217 (2021).
- [47] J. Hagel, S. Brem, and E. Malic, 2D Mater. **10**, 014013 (2022).
- [48] L. Sponfeldner, N. Leisgang, S. Shree, I. Paradisanos, K. Watanabe, T. Taniguchi, C. Robert, D. Lagarde, A. Balocchi, X. Marie, I. C. Gerber, B. Urbaszek, and R. J. Warburton, Phys. Rev. Lett. **129**, 107401 (2022).
- [49] A. Raja, A. Chaves, J. Yu, G. Arefe, H. M. Hill, A. F. Rigosi, T. C. Berkelbach, P. Nagler, C. Schüller, T. Korn, *et al.*, Nat. Commun. **8**, 15251 (2017).
- [50] K. Liu, L. Zhang, T. Cao, C. Jin, D. Qiu, Q. Zhou, A. Zettl, P. Yang, S. G. Louie, and F. Wang, Nat. Commun. **5**, 1 (2014).
- [51] H. Zheng, D. Zhai, and W. Yao, Nano Lett. **22**, 5466–5472 (2022).
- [52] A. Arora, M. Koperski, A. Slobodeniuk, K. Nogajewski, R. Schmidt, R. Schneider, M. R. Molas, S. M. de Vasconcellos, R. Bratschitsch, and M. Potemski, 2D Mater. **6**, 015010 (2018).
- [53] T. Deilmann, P. Krüger, and M. Rohlfing, Phys. Rev. Lett. **124**, 226402 (2020).
- [54] G. Aivazian, Z. Gong, A. M. Jones, R.-L. Chu, J. Yan, D. G. Mandrus, C. Zhang, D. Cobden, W. Yao, and X. Xu, Nat. Phys. **11**, 148 (2015).
- [55] M. Goryca, J. Li, A. V. Stier, T. Taniguchi, K. Watanabe, E. Courtade, S. Shree, C. Robert, B. Urbaszek, X. Marie, *et al.*, Nat. Commun. **10**, 4172 (2019).
- [56] A. Arora, Journal of Applied Physics **129**, 120902 (2021).
- [57] A. Kormányos, G. Burkard, M. Gmitra, J. Fabian, V. Zólyomi, N. D. Drummond, and V. Fal'ko, 2D Mater. **2**, 022001 (2015).
- [58] M. Brotons-Gisbert, A. Segura, R. Robles, E. Canadell, P. Ordejón, and J. F. Sánchez-Royo, Phys. Rev. Mater. **2**, 054602 (2018).
- [59] E. Liu, J. van Baren, Z. Lu, T. Taniguchi, K. Watanabe, D. Smirnov, Y.-C. Chang, and C. H. Lui, Nat. Commun. **12**, 6131 (2021).